Journal of Thermal Analysis and Calorimetry (2023) 148:12421–12432
https://doi.org/10.1007/s10973-023-12560-z

A study on the abnormal thermal behaviors of barkinite by ReaxFF molecular dynamics simulation

Shaoqing Wang[1] · Xiaoling Wang[1] · Yungang Zhao[1] · Yuhan Lin[1]

Received: 14 November 2022 / Accepted: 10 September 2023 / Published online: 28 October 2023

Abstract
Barkinite is termed as a maceral in the Chinese bituminous coal, but it has not been recognized by International Committee for Coal and Organic Petrology, which is related to the unclear chemical structure of barkinite. The abnormal thermal behaviors of barkinite/bark coal were reported in our previous works, but the reason is not fully understood. For discussing these issues, the chemical structural model of barkinite with a molecular formula of $C_{128}H_{166}N_2O_{11}$ was constructed by elemental analysis, ^{13}C nuclear magnetic resonance spectroscopy, and Fourier transform infrared spectroscopy. Besides, a heat up simulation of barkinite model was also performed by ReaxFF. The results showed that the chemical structural model of barkinite has long aliphatic chains and many hydroxyl and ether functional groups, which act as side chains and bridges. Naphthalene is main aromatic unit. When barkinite model system was heated from 300 to 2850 K, the change trends of pyrolysis products were described from four pyrolysis stages. The most noticeable changes of tar yields occurred in the simulated temperature range of 2100–2600 K, which caused the abnormal thermal behaviors of barkinite. According to the reaction pathways, the formation of tar products is related to the cleavage of aliphatic chains and the recombination of small molecular free radicals.

Keywords Barkinite · Molecular structural model · Abnormal thermal behaviors · ReaxFF

Introduction

Barkinite, termed as a maceral in Chinese bituminous coal maceral classification, was described to derive from the cortex tissue of stem and root of plants, in which the cell wall and filling material apparently have become impregnated with suberin substances [1]. It has some obvious optical characteristics, as pointed out by Sun et al. [2] and Zhong et al. [3], which are different with those of suberinite and cutinite. In the classification of liptinite-ICCP system 1994 [4], barkinite was cited when introducing suberinite maceral. However, barkinite has not been recognized as a maceral by ICCP. Hower et al. [5] also pointed out that it was more appropriate to use the term "component" instead of "maceral" for barkinite. One of reasons is that the chemical structural characteristics of barkinite are unclear when compared with others liptinite macerals, especially suberinite and cutinite. Barkinite was found in the Late Permian coals in the Southern China, for examples, in Leping coalfield, Changguang coalfield, and Shuicheng coalfield.

Several advanced characterization techniques have been widely used to study the composition and structure of coal [6–13]. Various analytical methods were used to discuss the chemical structural information of barkinite, for instance, Fourier transform infrared spectroscopy (FTIR), Carbon–13 nuclear magnetic resonance (^{13}C–NMR), High-resolution transmission electron microscopy (HRTEM), and Atomic force microscopy (AFM) [14–17]. The most interesting data on the chemical structure of barkinite were obtained in our working group. Combined with the previous studies [15–17], the characteristics of aliphatic groups and aromatic groups of barkinite have been described qualitatively. But the chemical structural model of barkinite is still in vague, which limited the understanding on barkinite. Furthermore, when the content of barkinite is close to 30%, the abnormal thermal behaviors of the coal rich in barkinite were presented: an extensive thermal decomposition and extra-high fluidity [18–20]. Considering the special thermal behaviors and properties, some effective utilization ways for bark coal/barkinite were suggested by

✉ Shaoqing Wang
wangzq@cumtb.edu.cn

[1] College of Geoscience and Surveying Engineering, China University of Mining and Technology (Beijing), D11, Xueyuan Road100083, Beijing, China

our working group, including low-temperature carbonization, co-coking, direct liquefaction, co-processing, and hydrogen production [21]. For more effective use of bark coal/barkinite, the reason for thermal behaviors and properties was discussed depending on the chemical structure of barkinite [22]. But the abnormal thermal behaviors of barkinite still cannot be clearly explained by experimental techniques because of the heterogeneity of barkinite and the complexity of the pyrolysis process, which limited the further utilization of bark coal/barkinite [23]. Meanwhile, the change trends of pyrolysis products of barkinite when heating are also unclear. Fortunately, the strategy of computer molecular simulation technology combined with coal/maceral models provides a new solution to this issue.

Recently, molecular dynamics combined with ReaxFF reaction force field (ReaxFF-MD) provides a promising method for exploring complex chemical reactions and multiple reaction pathways in large-scale systems. The calculation accuracy of ReaxFF – MD method is close to Density Functional Theory (DFT) method but with much reduced computational costs [24–29]. Especially, ReaxFF-MD method has been successfully used to simulate and explore the reaction process of coal [25–32]. For describing the pyrolysis process of coal, Salmon et al. first used the ReaxFF reaction force field to perform reactive dynamics simulations on a macro-model of Morwell Brown coal and found that these reactive MD simulations successfully reproduced the thermal decomposition process observed in various experimental studies, including defunctionalization, depolymerization, and rearrangement of residual structures [25]. Zheng et al. [27] investigated the entire stage of coal pyrolysis by performing ReaxFF-MD simulation on a large-scale model of Liulin bituminous coal.[27] The results showed that the Liulin coal pyrolysis process can be divided into four stages: the activation stage, the primary pyrolysis stage, the secondary pyrolysis stage, and the recombination dominated stage. For examining structural modifications and reactions associated with coal pyrolysis, Castro–Marcano et al. [29] employed the ReaxFF reactive force field to perform pyrolysis simulations on a large-scale molecular model of Illinois no. 6 coal. The results showed that Illinois coal pyrolysis was mainly initiated by the release of hydroxyl groups, the dehydrogenation of hydroaromatic structures, and the cleavage of heteroatom-containing cross-links. Meanwhile, the main pyrolysis products were in agreement with experimental data. Also based on reaction molecular dynamics simulations, Hong et al. [30, 31] and Xu et al. [32] simulated the pyrolysis process for various coals. These studies showed that ReaxFF-MD method is reliable for simulating coal pyrolysis process. Therefore, ReaxFF-MD method has great potential in exploring the abnormal thermal behaviors of barkinite.

Considering the special chemical structure and thermal behaviors of barkinite [15–21], it is difficult to observe in situ the change of barkinite when heating. So the aims of this work were: (1) to build a chemical structural model of barkinite, (2) to simulate the change process of barkinite heated, and (3) to make an explanation on the abnormal thermal properties of barkinite, especially at 430–450 °C.

Sample and methods

Sample and preparation

Bark coal sample was selected from the B_3 coal seam in the Mingshan coal mine, Jiangxi province, in Southern China. Barkinite was separated by density gradient centrifugation (DGC) method combining with hand picking. The detailed procedure for barkinite separation was described in the work of Guo et al. [33]. The purity of barkinite separated is above 95 vol. %.

Analytical methods

Ultimate and proximate analyses, FTIR, and ^{13}C NMR data were utilized to characterize the structure and composition of coal. The ultimate and proximate analyses of barkinite were obtained from the works of Wang et al. [21]. The detailed information of FTIR and ^{13}C NMR data was introduced in the paper of Wang et al. [15].

Proximate analysis and ultimate analysis were performed according to the methods of GB/T 212–2008, GB/T 476–2008, GB/T 214–2007, and GB/T 215–2003.

^{13}C NMR spectrum was obtained on a Varian Unity Inova 300 M NMR spectrometer with a double resonance probe by using cross-polarization and magic-angle-spinning (CP/MAS) techniques. The ^{13}C frequency was set to 75.5 MHz, and the spin rate was 12 kHz. The contact time was 0.005 s, and the recycle delay was 4 s.

FTIR measurement was carried out on a Nicolet model 6700 Fourier transform-infrared spectrometer. Barkinite sample of 1–3 mg was ground with 300 mg KBr for 2 min and then, pressed into a pellet in an evacuated die under a pressure of 10 MPa for 2 min. FTIR spectrum was recorded with 300 scans at a resolution of 2 cm^{-1} in the wavenumber range of 4000–400 cm^{-1}.

Model construction method

In this study, the chemical structural model of barkinite was constructed using the model construction method proposed by Xiang et al. [34]. First, a initial two-dimensional (2D) structural model of barkinite was drawn using ChemSketch software based on elemental composition, FTIR, and ^{13}C NMR analysis data. Then, the element composition, aromaticity, and ^{13}C NMR spectrum of the 2D structural model of barkinite calculated by the ACD predictor were compared with experimental results to verify the rationality of the model. Until the calculated results of the model are

consistent with the experimental results, the final 2D structural model of barkinite is determined.

Next, 2D structural model was optimized by geometry optimization and annealing dynamics simulation to obtain the optimal three-dimensional (3D) structural model of barkinite. All simulations are completed by using Forcite module of Materials studio. Geometry optimization was first performed on the 2D structural model of barkinite by using the Dreiding force field with the smart minimizer method. The convergence tolerance of energy and force was 0.001 kcal mol^{-1} and 0.5 kcal mol^{-1} $Å^{-1}$, respectively. The maximum number of iteration steps is 5000, and the QEq method was chosen to balance atomic charges. Subsequently, in the NVT ensemble, the annealing dynamics simulations were performed with a time step of 1 fs to overcome the molecular structure energy barrier. The initial and final temperatures were both set to 300 K, while the mid-cycle temperatures was set to 700 K. The heating and cooling rates were both set at 40 K $time^{-1}$. The total number of cycles is 15. The Nosé–Hoover–Langevin (NHL) thermostat method was applied for controlling the temperature. The total number of steps was set as 300,000 to search the lowest-energy conformation. Geometry optimization is adopted again to optimize the model after each cycle. The van der Waals interactions and electrostatic interactions in all simulations were calculated by the Atom-based method.

ReaxFF force field and simulation details

ReaxFF is a reactive force field based on the bond order principle, which relates the bond energy to bond lengths, valence angles and torsion angle [35–37]. ReaxFF combines the advantages of quantum mechanics and classical molecular dynamics, allowing to simulate the reaction process of complex systems with thousands of atoms. The ReaxFF-MD simulation was performed by the ReaxFF program developed by van Duin et al. [38]. More detailed description of the ReaxFF force field can be found elsewhere [38]. The H/C/O/N/S/B force field parameters were adopted in this study [37, 39]. A Berendsen thermostat with a damping constant of 0.1 ps was used to keep the temperature in equilibrium in all ReaxFF-MD simulations.

Before simulating the pyrolysis of barkinite, a macromolecular model system was constructed. The 2D barkinite structural model was optimized by Forcite module with the Dreiding force field in the Materials Studio software. Five optimized structural models were randomly assembled into a $50 \times 50 \times 50$ Å periodic cell at a low density of 0.1267 g cm^{-3}. The lower initial density of the periodic cell was helpful to prevent overlapping of aromatic layers in the final structure. This initial model system was further optimized through the energy minimization method. The model system was equilibrated at 300 K for 10 ps using NVT ensemble. For complying with the actual density of barkinite, the density of barkinite model system was adjusted to 1.20 g cm^{-3} using NPT ensemble. The system was relaxed at 300 K using NVT ensemble to avoid any reaction. To discuss the product distributions and reaction mechanism of barkinite upon heating, a heat up simulation was performed on the model system from 300 to 2850 K at rates of 5 K ps^{-1} using the "Velocity Verlet + Berendsen" method with a time step of 0.25 fs. It is worth mentioning that the higher temperature (300–2850 K) used in the ReaxFF MD simulation is higher than that employed in the laboratory experiment to allow the reactions to occur within picoseconds. Despite time and temperature between the simulations and experiments are different, good qualitative agreement on product distribution and chemical reaction mechanism was obtained in the literatures [25, 27, 29].

Results and discussion

Barkinite model construction

Various experimental techniques, such as solid-state ^{13}C NMR, FTIR, and ultimate analysis, can be effectively applied to explore the chemical structural characteristics of coal. The ultimate analysis data listed in Table 1 were used to determine the initial molecular formula of the barkinite model. The sulfur content with a value of 0.11% is low in Table 1, so sulfur was not considered in the model. Thus, nitrogen was chosen as the reference standard. The initial molecular formula of the barkinite model can be expressed as $(C_{61}H_{62}NO_{5.5})_n$. It is worth emphasizing that the barkinite does not exhibit a definite molecular mass in this study. Therefore, the average molecular size (or molecular mass) of barkinite should be assumed to construct a reasonable structural model with complex structure. In view of the limitation of the ACD/NMR predictor on the number of carbon atoms, three molecular formulas with different sizes for barkinite structural model are available for selection, that is, the corresponding parameters n are assigned to 1, 2, and 3, respectively. When the parameter n was equal to 1,

Table 1 Proximate and ultimate analysis of barkinite [21]

Sample	Proximate analysis/mass%, daf			Ultimate analysis/mass%, daf				
	M_{ad}	A_d	V_{daf}	C_{daf}	H_{daf}	N_{daf}	$S_{t,daf}$	O_{daf}*
Barkinite	0.71	0.97	62.16	81.59	6.91	1.57	0.11	9.82

the molecular formula of the smallest size ($C_{61}H_{62}NO_{5.5}$) is obtained. However, because its size is too small to reflect the complex structure of barkinite, $C_{61}H_{62}NO_{5.5}$ was excluded in this study. If parameter n equal to 3, $(C_{61}H_{62}NO_{5.5})_3$ is the molecular formula of the largest size. The larger the molecular size, the greater the computational cost for ReaxFF-MD simulations. So this will cause expensive computational cost for the subsequent ReaxFF-MD simulation. Therefore, it is considered appropriately that the initial molecular formula is $(C_{61}H_{62}NO_{5.5})_2$ in this study. Additionally, the molecular size of the barkinite model also showed the same order of magnitude as those macerals reported previously [41–44].

M_{ad}, moisture on an air-dried basis; A_d, ash on a dry basis; V_{daf}, volatile matter on a dry and ash-free basis; S_t, total sulfur; mass%, daf, mass percentage of various elements on a dry and ash-free basis.

* By difference.

^{13}C NMR data were used to provide information on the carbon skeleton structure [45–49]. To quantify the relative proportion of different types of carbons in the skeleton structures of barkinite, the ^{13}C NMR spectrum was fitted with the Origin 7.5 software based on the chemical shift of specific bonds [50–53]. The ^{13}C NMR peak fitting curve of barkinite is shown in Fig. 1. The ^{13}C NMR structure parameters of barkinite are calculated based on the integrated relative areas of each sub-peak in the ^{13}C NMR fitting results, as shown in Table 2. From Table 2, the fraction of aliphatic carbons (f_{al}) is 53.13%, which indicates that aliphatic structures are the main structures in the structural model of barkinite. The fraction of methylene carbons (f_{al}^{H}) is 18.87%, which means that methylene is the largest proportion in the aliphatic carbons. Average methylene chain length (C_n) was calculated to estimate the aliphatic chain length. The C_n value of barkinite is 2.47 (equal to f_{al}^{H}/f_{ar}^{C}), which indicates that the aliphatic chain in the barkinite is longer. The mole fraction of aromatic bridgehead carbons (X_{BP}) is an important parameter

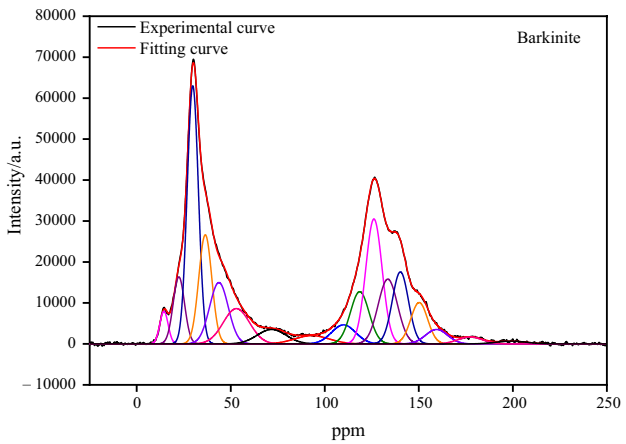

Fig. 1 ^{13}C NMR fitting curve of barkinite

Table 2 13C NMR structural parameters of barkinite.

Structure fragments	Symbol	Chemical shift/ppm	Relative area/%
Aliphatic methyl	f_{al}^{M}	14–16	1.77
Aromatic methyl	f_{al}^{A}	16–22	4.99
Methylene	f_{al}^{H}	22–36	18.87
Methine and Quaternary	f_{al}^{D}	36–50	9.34
Oxy-aliphatic	f_{al}^{O}	50–95	10.67
Total aliphatic	f_{al}	0–95	53.13
Aromatic protonated	f_{ar}^{H}	95–129	22.74
Aromatic non-protonated	f_{ar}^{N}	129–160	22.48
Aromatic bridgehead	f_{ar}^{B}	129–138	8.22
Aromatic branched	f_{ar}^{C}	138–148	7.62
Oxy–aromatic	f_{ar}^{O}	148–165	6.64
Total aromatic	f_{ar}	95–165	45.22
Carboxyl	f_{a}^{C}	165–180	1.12
Carbonyl	f_{a}^{O}	180–220	0.55

for estimating the aromatic cluster size. The X_{BP} value of barkinite is 0.18 (equal to f_a^B/f_a), which is close to 0.20 of naphthalene. This indicates that the aromatic unit in the barkinite is mainly in the form of naphthalene. Some ^{13}C NMR structural parameters were used to determine the different types of carbon skeleton structures in the model. For instance, the number of carboxyl groups is approximately equal to 1 by multiplying the fraction of carboxyl (f_a^C) by the total number of carbon atoms. Similarly, the numbers of aromatic carbons and aliphatic carbons are approximately equal to 55 and 65, respectively.

Figure 2 shows the FTIR spectrum of the barkinite. As shown in Fig. 2, the FTIR spectrum was divided into four bands: 700–900 cm^{-1}, 1000–1800 cm^{-1}, 2800–3000 cm^{-1} and 3000–3600 cm^{-1}. Among them, the bands at 1000–1800 cm^{-1} and 2800–3000 cm^{-1} bands were assigned to oxygen functional groups and alkyl functional groups, respectively. To obtain the semi-quantitative information on oxygen functional groups and alkyl functional groups of barkinite, the FTIR spectrum in the 1000–1800 cm^{-1} and 2800–3000 cm^{-1} bands was fitted with Origin 7.5 software. Fitting results are present in the Support information (Fig. S1 and S2, Table S1 and S2). The distribution ratios of different groups in the oxygen functional groups and alkyl functional groups of barkinite were obtained by FTIR fitting results. As shown in Fig. 3, oxygen functional groups in the barkinite are mainly hydroxyl groups (or/and ethers), followed by carbonyl and carboxyl groups, the ratio of which is approximately 8:1:1. Methylene groups are the major alkyl functional groups, followed by methyl and methine groups, and the ratio of the three is close to 6:2:1. Pyrrole

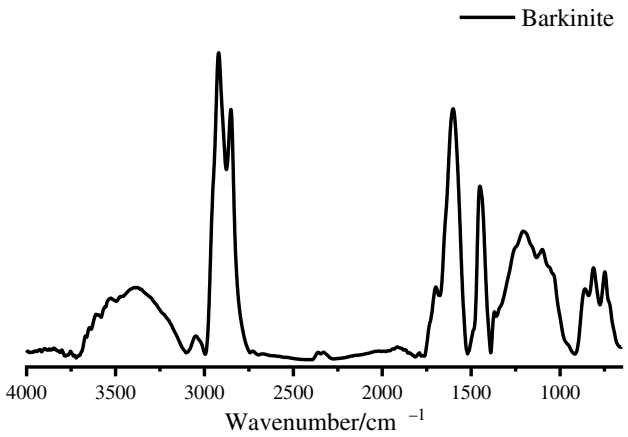

Fig. 2 FTIR spectrum of Barkinite [15]

and pyridine are the two major nitrogen forms in coal and maceral [48, 54, 55]. Thus, two nitrogen atoms in this study were assigned to pyridine and pyrrole, respectively.

Based on the above structural information, the initial barkinite model was assembled with various molecular fragments. For adjusting the barkinite model, the ^{13}C NMR spectrum, element composition, and aromaticity were calculated by ACD/C NMR Predictor. The ACD/C NMR predictor software package was developed by Advanced Chemistry Development Corporation for calculating ^{13}C NMR chemical shifts of organic structures [56, 57]. The chemical shifts of the model structures were calculated by searching the ACD/CNMR software database for similar substructure fragments with corresponding experimental shift values and then evaluating their chemical shift values [56]. Meanwhile, this process takes into account intramolecular interactions. The ^{13}C NMR spectra of the model structures were obtained by setting an adequate linewidth for each peak and summation. After several adjustments on the position of various structural units, the 2D structural model of barkinite was considered reasonable until the calculated results match the experimental results. The calculated spectrum is basically consistent with the experimental spectrum, as shown in Fig. 4. The model structure parameters and the experimental structure parameters of barkinite are listed in Table 3. From Table 3, the element composition and aromaticity of barkinite model are basically consistent with the experimental values. Here, there is a slight and unavoidable difference between the final and initial molecular formula of the model ($C_{128}H_{166}N_2O_{11}$and $C_{122}H_{124}N_2O_{11}$), which is caused by the model adjustment. For obtaining the lowest-energy conformation, the final 2D structural model of barkinite was optimized by geometry optimization and annealing dynamics

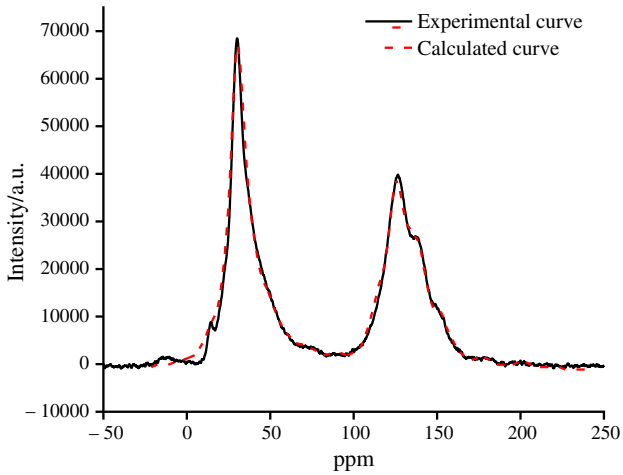

Fig. 4 Experimental and calculated ^{13}C NMR curve of barkinite

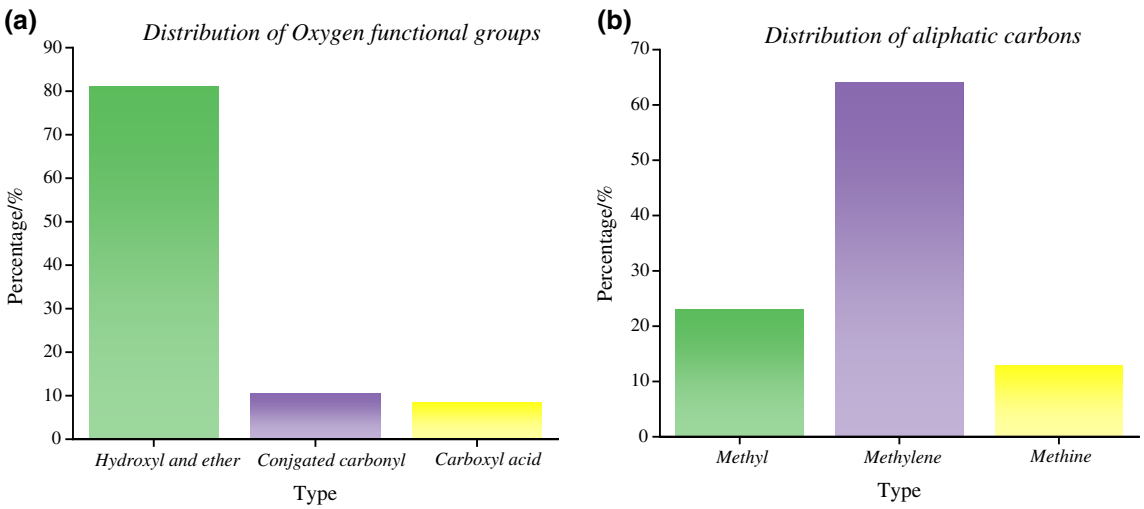

Fig. 3 Distribution of oxygen functional groups (a) and aliphatic carbons (b) based on FTIR analysis results

Table 3 Model and experimental structure parameters of barkinite

Sample	Molecular formula	Molecular mass	Ultimate analysis		Aromaticity	
			Model	Experiment	Model	Experiment
Barkinite	$C_{128}H_{166}N_2O_{11}$	1906	C(80.55%)H(8.77%) N(1.47%)O(9.22%)	C(81.59%)H(6.91%) N(1.57%) O(9.82%)S(0.11%)	0.45	0.45

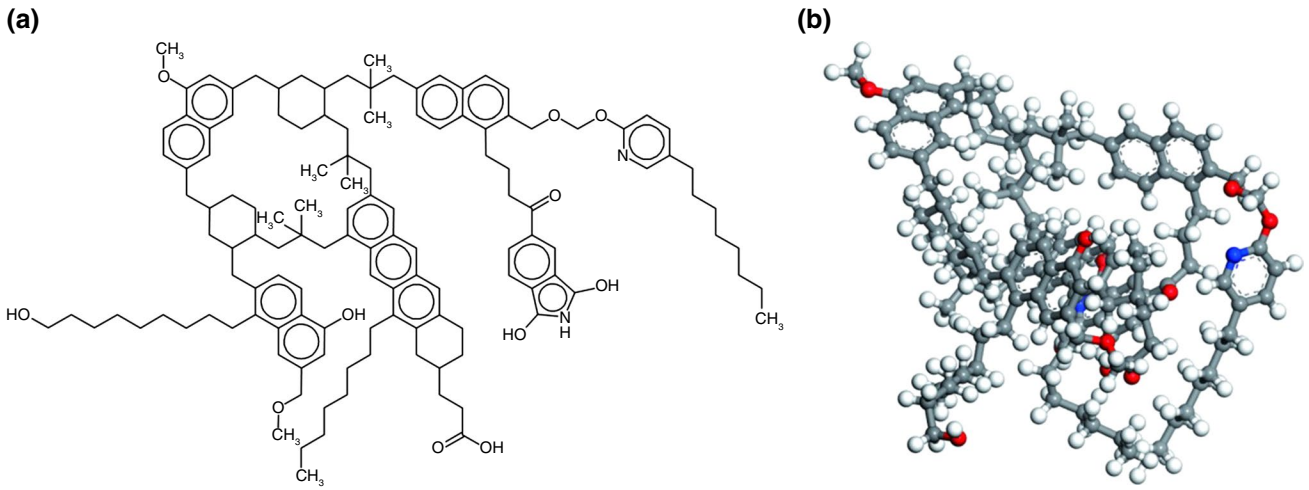

Fig. 5 2D **a** and 3D **b** chemical structural model of barkinite. (Gray atom: carbon; White atom: hydrogen; Red atom: oxygen; Blue atom: nitrogen)

simulation. The final structural model of barkinite is shown in Fig. 5. From Fig. 5a, the structural model of barkinite has long aliphatic chains and many hydroxyl and ether functional groups, which serves as bridge bonds and side chains in the model. The aromatic structure is mainly composed of naphthalene. The 3D structural model of barkinite shows a good spatial configuration, as shown in Fig. 5b.

Analysis of heat up simulation of barkinite model

To explain the abnormal thermal behaviors of barkinite, a heat up simulation was finally determined and performed from 300 to 2850 K at a heating rate of 5 K ps^{-1} by repeating the simulation several times. Meanwhile, the rationality of the barkinite model was further verified by comparing simulated result and experimental thermogravimetric (TG) curves, as shown in Fig. 6. In the TG experiment, the barkinite sample was heated from 25 to 900 °C at a heating rate of 10 °C min^{-1}. From Fig. 6, the simulation temperature (1350–2850 K) is much higher than the temperature (25–900 ℃) of TG, because the simulated time scale (on the order of picoseconds) is greatly shorter than the real time in experiments (on the order of seconds) [58, 59]. In other words, increasing the simulation temperature can significantly

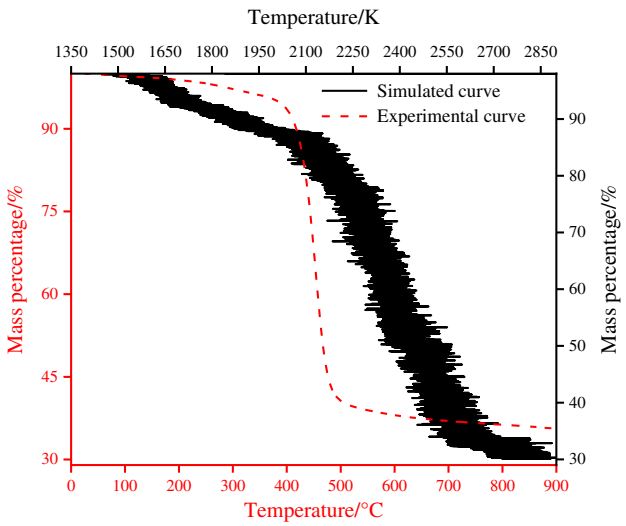

Fig. 6 Comparison of simulated result and experimental TG curves of barkinite model

increase the reaction rate and has no significant effect on the reaction type in the ReaxFF simulation [60]. Therefore, ReaxFF-MD simulation often shortens the reaction time by increasing the reaction temperature. Here, the change trend

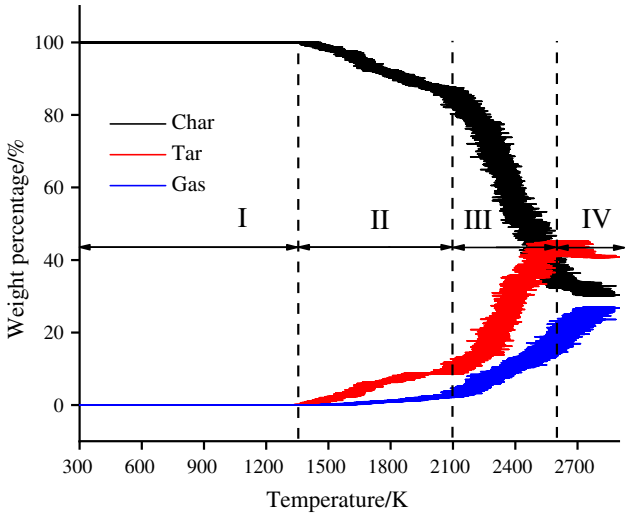

Fig. 7 Change trend of pyrolysis products of barkinite

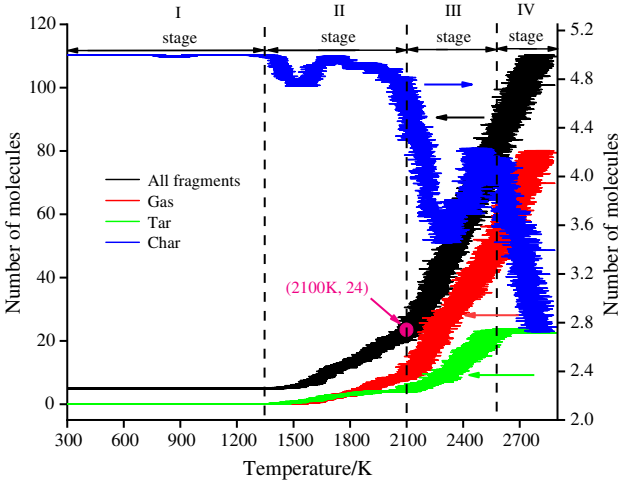

Fig. 8 Number of pyrolysis products fragments in pyrolysis simulation from 300 to 2850 K

of char yield accompanies with temperature obtained from ReaxFF-MD simulation roughly agrees with the trend in the experimental result, which indicates that the pyrolysis simulation of the barkinite model can qualitatively predict the changes of pyrolysis products in the laboratory experiment. This provides strong evidence for the applicability of the proposed barkinite model. The simulated temperature ranges of 1350–2850 K at a heating rate of 5 K ps^{-1} roughly correspond to the experimental temperature range of 25–900 °C at a heating rate of 10 °C min^{-1}.

Based on the number of carbon atoms, the products obtained from the pyrolysis simulation can be classified as gas, tar, and char [26, 61, 62]. C_{40+} compounds with more than 40 carbon atoms are considered as char. C_5–C_{40} compounds with 5–40 carbon atoms are considered as tar. C_0–C_4 compounds with less than 5 carbon atoms are considered as gas. Tar includes heavy tar (C_{14}–C_{40} compounds) and light tar (C_5–C_{13} compounds). The change trends of the mass percentage and molecule number of pyrolysis products with the temperature rising from 300 to 2850 K are shown in Figs. 7 and 8, respectively. Based on the changing trend of pyrolysis products, at least four stages were described.

The first stage is from 300 to 1350 K (stage I), where the barkinite model system shows almost no mass loss, and the number of molecules is basically unchanged, which indicates that almost no thermal decomposition reaction occurs. However, due to the rising temperature, the conformation and potential energy of the barkinite model were changed. Figure 9 shows the snapshots of the barkinite configuration at different temperatures (300 K and 1350 K) in the ReaxFF-MD simulation. When the temperature rises to 1350 K, the barkinite molecules break through the barrier of structural potential energy by absorbing enough heat, thereby triggering chemical reactions.

As temperature rises from 1350 to 2100 K (stage II), the molecular structure of barkinite undergoes thermal decomposition, resulting in a small number of free radical structures and fragments, which include gas, tar, and char. The char yield decreases slowly with increasing temperature, while the tar yield increases slowly. The gas yield only increases slightly. The high temperature can provide enough energy to break the weak bond, such as ether bond, so that the maximum number of molecular fragments reached 24 in this stage, as shown in Fig. 8.

As temperature continues to increase from 2100 to 2600 K (stage III), the char yield decreases rapidly, while the yields of tar and gas increases rapidly. The number of char fragments first decreases rapidly and then increases rapidly, and that of tar fragments and gas fragments increased rapidly, as shown in Fig. 8. This indicates that most of the reactions at this stage are possible related to the decomposition of char. Meanwhile, due to the complexity of the barkinite structure and the uncertainty of pyrolysis, there may be multiple thermal decomposition modes of the barkinite at this stage. At 2600 K, the yields of char and tar achieved the minimum and the maximum values, respectively.

With the temperature increasing from 2600 to 2850 K (stage IV), the char yield remains essentially constant with increasing temperature, while the tar yield decreases slightly. Besides, the gas yield increases rapidly. The number of gas fragments increases at this stage, but the number of char fragments decreases, while that of tar fragments basically remain equilibrium state, which indicates that the thermal decomposition and recombination reactions of the molecules or radical fragments are the two main events at this stage [27, 63]. The thermal decomposition reactions mainly occurred in which the old tar fragments were decomposed into new tar fragments and gas molecules. The recombination reactions

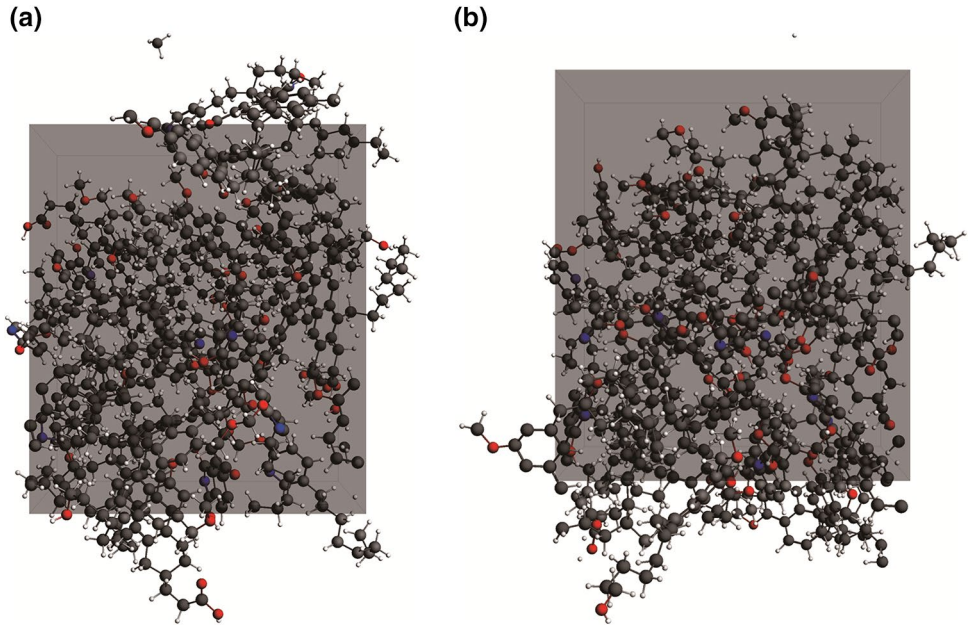

Fig. 9 Snapshots of initial and intermediate configurations in the ReaxFF-MD simulation: initial configuration at 300 K (**a**) and intermediate configuration at 1350 K (**b**)

mainly occurred in which two or more old char fragments combine to form new larger char fragments.

Analysis of Abnormal Thermal Behaviors of Barkinite

Bark coal is named as being high barkinite content, and it also is a humic coal. As reported in the previous works of our working group[18–21] and other results[64–66], the barkinite/bark coal has some abnormal thermal behavior. When barkinite was heated, the maximum rate of mass loss of barkinite reached to 1.11% $°C^{-1}$ at the heating rate of 10 °C/min. For Gieseler thermoplastic property, the values of the maximum fluidity of bark coal were 30,000 dial divisions per minute (ddpm), even more than 180,000 (ddpm), which exceeded the limitation of experimental instrument used. The temperature of maximum fluidity is about 440 °C. Barkinite has a good hydrocarbon generation potential [64, 65] and liquefaction behavior [20, 66]. The liquefaction conversion ranges were 87–91%, and the oil yield were 58–60%.

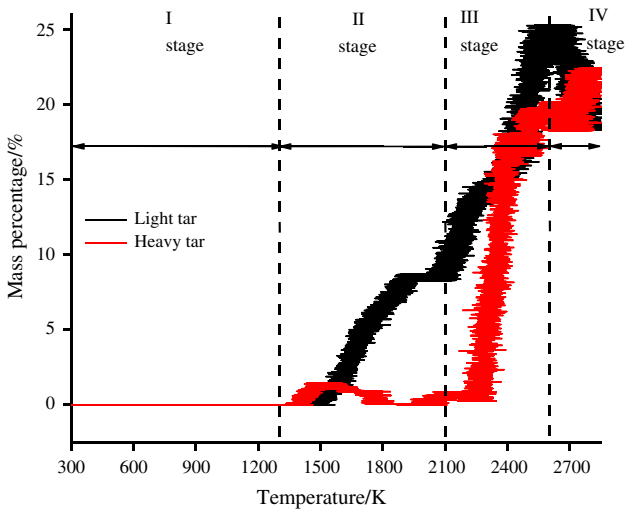

Fig. 10 Change trend of tar products of barkinite

These abnormal thermal behaviors of bark coal/barkinite were discussed from the chemical structural characteristics and barkinite content [16–22], which provide a good explanation on their behaviors. However, the explanation on its abnormal thermal behaviors is still insufficient. In this work, the chemical structure model of barkinite was constructed and the pyrolysis process of barkinite at a heating rate of 5 K ps^{-1} was simulated, and these information are helpful to further explore the abnormal thermal behaviors of bark coal/barkinite.

According to Figs. 7 and 8, as the barkinite model system was heated from 300 to 2100 K, the yield and number of tar components increased gradually, and that of char components decreased gradually. But when temperatures are at 2100–2600 K, the char yield decreased rapidly, and the tar yield increased rapidly. Furthermore, at the temperature of 2600 K, the maximum values of tar yield were obtained, while the value of char yield is the minimum. This is possible the reason why barkinite has intensive thermal decomposition, and at about 450 °C, the maximum rate of thermal decomposition is arrived.

Bark coal has high Gieseler thermoplastic property, especially for bark coal with high barkinite content [18–20]. The higher barkinite content, the more abnormal the Gieseler thermoplastic property of bark coal. Even for barkinite content reach to 80%, no solidification temperature was obtained

[18]. As shown in Fig. 7, from 1350 to 2100 K, the tar content increased gradually and the content of char decreased gradually. When the temperature rises in the temperature range of 2100–2600 K, the content of tar increased rapidly, while the content of char decreased rapidly. In particular, the content of the heavy tar increases rapidly in the temperature range of 2100–2600 K, as pointed out in Fig. 10. Furthermore, the number of tar fragments also increased rapidly at this temperature range (Fig. 8). As pointed out by Ouchi et al. [64], low molecular mass products that play an important role in thermoplasticity are derived from the coal chemical network, named by the γ–compound theory. Therefore, the large amount of tars produced in this temperature range, especially heavy tars, are possible related to the abnormal Gieseler thermoplastic behavior of bark coal.

For gaining further insight into the abnormal thermal behaviors of barkinite, the formation pathways of typical tar products (including light tar and heavy tar) in the temperature range of 2100 to 2600 K are shown in Fig. 11. From Fig. 11a to d, the formation of pyrolysis tar products not only results from the decomposition of large molecules, but also from the recombination of small molecular free radicals. With the continuously increasing temperature, the previously formed radicals underwent new cleavage and recombination processes, forming a wider variety of tar products. Finally, the tar yield reached its maximum value at 2600 K, as shown in Fig. 7. These reaction pathways indicated that the formation of pyrolysis tar products of barkinite model system is related to the cleavage of aliphatic chains (especially methylene chains) and the recombination of small

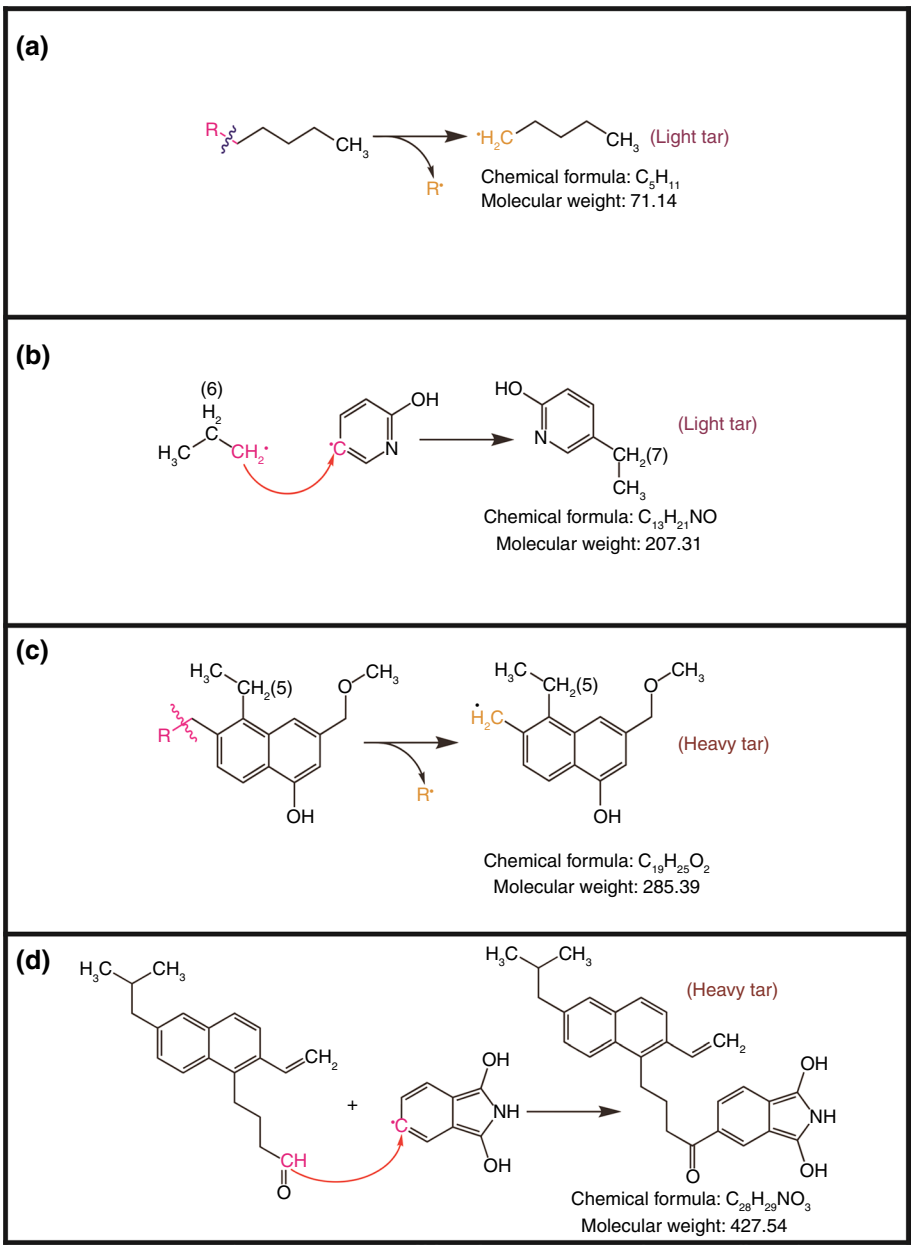

Fig. 11 Formation pathways of typical tar products of barkinite between 2100 and 2600 K

molecular free radical fragments, which cause the abnormal thermal behaviors of the barkinite between 400 °C and 500 °C.

Conclusions

The chemical structural model of barkinite was constructed, and the distribution of the pyrolysis products of barkinite in the temperature range of 300–2850 K was obtained by ReaxFF-MD simulation. The general conclusions obtained are as following:

The chemical structural model of barkinite has long aliphatic chains and many hydroxyl and ether functional groups, which act as side chains and bridges. The aromatic structure is mainly composed of naphthalene. The molecular formula of barkinite structural model is $C_{128}H_{166}N_2O_{11}$. The ^{13}C NMR spectrum, elemental composition, aromaticity, and TG curve of barkinite model are basically consistent with the experimental results.

The simulated pyrolysis process of barkinite can be described from four stages. The stage I range from 300 to 1350 K, where no obvious change was occurred. As the temperature continues to increases from 1350 to 2100 K (stage II), the char yield decreases slowly, while the tar yield increases slowly. The noticeable changes of char and tar yields were happened at the stage III (from 2100 to 2600 K). The char yield decreases rapidly, while the yields of tar and gas increase rapidly. At 2600 K, the minimum and the maximum yields of char and tar were reached, respectively. The last stage (stage IV) occurred in the temperature range from 2600 to 2850 K. At this stage, the char yield is basically unchanged, while the tar yield decreases slightly.

The abnormal thermal behaviors of barkinite/bark coal were explained based on the pyrolysis simulation results of barkinite model. The intensive thermal decomposition and high Gieseler fluidity are possible related to the change characteristics of tar products in the temperature range of 2100–2600 K, as shown in the pyrolysis simulation results of barkinite model. Besides, the formation of tar products of barkinite model system is related to the cleavage of aliphatic chains (especially methylene chains) and the recombination of small molecular radical compounds.

Supplementary Information The online version contains supplementary material available at https://doi.org/10.1007/s10973-023-12560-z.

Acknowledgements We gratefully thank the National Natural Science Foundation of China (Research Project No. 41472132; 42030807).

Author's contributions SW contributed to conceptualization, methodology, project administration, validation, writing—original draft, writing—review & editing, supervision, funding acquisition. XW contributed to methodology, software, validation, formal analysis, investigation, writing—original draft, writing—review & editing. YZ contributed to methodology, software, validation, formal analysis, investigation, writing—original draft, writing—review & editing. YL contributed to investigation, validation, and software.

Declarations

Conflict of interest The authors declare no competing financial interest.

References

1. Standardization Administration of China . Classification of macerals for bituminous coal (GB/T 15588–2001). Standards press of China: Beijing,2001, 1–7
2. Sun YZ, Horsfield B. Comparison of the geochemical characteristics of "barkinite"and other macerals from the Dahe mine. South China Energy Explor Exploit. 2005;23(6):475–94.
3. Zhong NN, Smyth M. Striking liptinitic bark remains peculiar to some Late Permian Chinese coals. Int J Coal Geol. 1997;33(4):333–49.
4. Pickel W, Kus J, Flores D, Kalaitzidis S, Christanis K, Cardotte BJ, Misz-Kennan M, Rodrigues S, Hentschel A, Hamor-Vido M, Crosdale P, Wagner N. Classification of liptinite–ICCP system 1994. Int J Coal Geol. 2017;169:40–61.
5. Hower JC, Suárez-Ruiz I, Mastalerz M, Cook AC. The investigation of chemical structure of coal macerals via transmitted–light FT–IR microscopy by X.Sun. Spectrochim Acta Part A. 2007;67:1433–7.
6. Strydom CA, Bunt JR, Schobert HH, Raghoo M. Changes to the organic functional groups of an inertinite rich medium rank bituminous coal during acid treatment processes. Fuel Process Technol. 2011;92(4):764–70.
7. Solum MS, Pugmire RJ, Grant DM. Carbon-13 solid-state NMR of Argonne-premium coals. Energy Fuels. 1989;3(2):187–93.
8. Jaiswal Y, Pal SL. Structural characterization of Indian vitrinite-rich bituminous Karharbari coal. ACS Omega. 2020;5(12):6336–47.
9. Jaiswal Y, Pal SL, Jain A, Kush L, Jaiswal H, Srivastava S. A multi-tool structural change investigation of Indian vitrinite rich bituminous coal due to CS_2/NMP interaction. J Mol Liq. 2021;323(1): 114599.
10. Lu L, Sahajwalla V, Kong C, Harris D. Quantitative X-ray diffraction analysis and its application to various coals. Carbon. 2001;39(12):1821–33.
11. Xu J, He QC, Xiong Z, Yu Y, Zhang S, Hu X, Jiang L, Su S, Hu S, Wang Y, Xiang J. Raman spectroscopy as a versatile tool for investigating thermochemical processing of coal, biomass, and wastes: recent advances and future perspectives. Energy Fuels. 2021;35(4):2870–913.
12. Yuan L, Liu QF, Mathews JP, Zhang H, Wu YK. Quantifying the structural transitions of Chinese coal to coal-derived natural graphite by XRD, raman spectroscopy, and HRTEM image analyses. Energy Fuels. 2021;35(3):2335–46.
13. Jaiswal Y, Pal SL, Jaiswal H, Jain A, Kush L, Rai D, Tatar D. An investigation of changes in structural parameters and organic functional groups of inertinite rich lignite during acid treatment processes. Energy Sources Part A. 2021: 1–18. https://doi.org/10.1080/15567036.2021.1923867.
14. Qin KZ, Guo SH, Huang DF, Li LY. Chemical structure and oil/gas potential of hydrocarbon source rock macerals as viewed by ^{13}C NMR techniques. Journal of The University of Petroleum, China. 1995;19:87–94 ((**in Chinese**)).

15. Wang SQ, Tang YG, Schobert HH, Guo YN, Su YF. FTIR and ^{13}C NMR Investigation of coal component of Late Permian coals from Southern China. Energy Fuels. 2011;25:5672–7.
16. Wang SQ, Tang YG, Schobert HH, Jiang D, Guo X, Huang F, Guo YN, Su YF. Chemical compositional and structural characteristics of Late Permian bark coals from Southern China. Fuel. 2014;126:116–21.
17. Wang SQ, Liu SM, Sun YB, Jiang D, Zhang XM. Investigation of coal components of Late Permian different ranks bark coal using AFM and Micro–FTIR. Fuel. 2017;187:51–7.
18. Wang SQ, Tang YG, Schobert HH, Mitchell GD, Liao FR, Liu ZZ. A thermal behavior study of Chinese coals with high hydrogen content. Int J Coal Geol. 2010;81:37–44.
19. Wang SQ, Tang YG, Schobert HH, Guo YN, Gao WC, Lu XK. FTIR and simultaneous TG/MS/FTIR study of Late Permian coals from Southern China. J Anal Appl Pyrol. 2013;100:75–80.
20. Wang SQ, Tang YG, Schobert HH, Jiang D, Sun YB, Guo YN, Su YF, Yang SP. Application and thermal properties of hydrogen–rich bark coal. Fuel. 2015;162:121–7.
21. Wang SQ, Wang DX, Tang YG, Sun YB, Jiang D, Su T. Study of pyrolysis behavior of hydrogen–rich bark coal by TGA and Py–GC/MS. J Anal Appl Pyrol. 2017;128:136–42.
22. Wang SQ, Chen H, Ma W, Liu PH, Yang ZD. Structural transformations of coal components upon heat treatment and explanation on their abnormal thermal behaviors. Energy Fuels. 2017;31(11):11587–93.
23. Wang SQ, Zhang XM, Lin YH, Sha YM. Hydrocarbon-generated potential of bark coal components from Southern China. J Therm Anal Calorim. 2019;135(6):3297–302.
24. Parr RG. Density functional theory. Chem Eng News. 1983;68:2470–84.
25. Salmon E, van Duin ACT, Lorant F, Marquaire PM, Goddard WA. Early maturation processes in coal. Part: 2 reactive dynamics simulations using the ReaxFF reactive force field on Morwell Brown coal structures. Org Geochem. 2009;40(12):1195–209.
26. Zheng M, Li XX, Liu J, Guo L. Initial chemical reaction simulation of coal pyrolysis via ReaxFF molecular dynamics. Energy Fuels. 2013;27(6):2942–51.
27. Zheng M, Li XX, Nie FG, Guo L. Investigation of overall pyrolysis stages for Liulin Bituminous coal by large–scale ReaxFF molecular dynamics. Energy Fuels. 2017;31(4):3675–83.
28. Zheng M, Pan Y, Wang Z, Li XX, Guo L. Capturing the dynamic profiles of products in Hailaer brown coal pyrolysis with reactive molecular simulations and experiments. Fuel. 2020;268: 117290.
29. Castro–Marcano F, Russo MF, van Duin ACT, Mathews JP. Pyrolysis of a large–scale molecular model for Illinois no. 6 coal using the ReaxFF reactive force field. J Anal Appl Pyrol. 2014;109:79–89.
30. Hong DK, Guo X. Molecular dynamics simulations of Zhundong coal pyrolysis using reactive force field. Fuel. 2017;210:58–66.
31. Hong DK, Li P, Si T, Guo X. ReaxFF simulations of the synergistic effect mechanisms during co–pyrolysis of coal and polyethylene/polystyrene. Energy. 2021;218: 119553.
32. Xu F, Liu H, Wang Q, Pan S, Zhao D, Liu Y. Study of non–isothermal pyrolysis mechanism of lignite using ReaxFF molecular dynamics simulations. Fuel. 2019;256: 115884.
33. Guo YN, Tang YG, Wang SQ, Li WW, Jia L. Maceral separation of bark coal and molecular structure study through high resolution TEM images. J China Coal Soc. 2013;38:1019–24 ((**in Chinese**)).
34. Xiang JH, Zeng FG, Liang HZ, Sun BL, Zhang L, Li MF, Jia JB. Model construction of the macromolecular structure of Yanzhou Coal and its molecular simulation. J Fuel Chem Technol. 2011;39(7):481–8 ((**in Chinese**)).
35. Brenner DW. Empirical potential for hydrocarbons for use in simulating the chemical vapour deposition of diamond films. Phys Rev B. 1990;42:9458–71.
36. Chenoweth K, van Duin ACT, Goddard WA. ReaxFF reactive force field for molecular dynamics simulations of hydrocarbon oxidation. J Phys Chem A. 2008;112:1040–53.
37. Bhoi S, Banerjee T, Mohanty K. Molecular dynamic simulation of spontaneous combustion and pyrolysis of brown coal using ReaxFF. Fuel. 2014;136:326–33.
38. van Duin ACT, Dasgupta S, Lorant F, Goddard WA. ReaxFF: a reactive force field for hydrocarbons. J Phys Chem A. 2001;105:9396–409.
39. Castro-Marcano F, Kamat AM, Russo MF, van Duin ACT, Mathews JP. Combustion of an Illinois No. 6 coal char simulated using an atomistic char representation and the ReaxFF reactive force field. Combust Flame. 2012;159:1272–85.
40. Gao MJ, Li XX, Guo L. Pyrolysis simulations of Fugu coal by large–scale ReaxFF molecular dynamics. Fuel Process Technol. 2018;178:197–205.
41. Liu L, Du ML, Fan JW, Li G, Cai YC. Embedded characteristics and macromolecular structure of sporinite of Pingdingshan coal in Early Permian. Energ Source Part A. 2019;2:1–14.
42. Du ML, Liu L, Fan JW, Li G, Schobert HH, Cai YC, Yang JL. Prediction and characterization of macromolecular structure of cutinite from luquan cutinitic liptobiolith with molecular simulation. Energ Source Part A. 2020; 1–16.
43. Lin HL, Wang YH, Gao SS, XueS Y, Yan CY, Han S. Chemical structural characteristics of high inertinite coal. Fuel. 2021;286: 119283.
44. Ping A, Xia WC, Peng YL, Xie GY. Construction of bituminous coal vitrinite and inertinite molecular assisted by ^{13}C NMR. FTIR and XPS J Mol Struct. 2020;1222: 128959.
45. Liu J, Yan CY, Zhang C, Wang AQ, Wang ZX, Xu YH, Feng L. Construction of the structure model of Zhaotong lignite skeleton by TG-GC/MS and 13C-NMR data. J Therm Anal Calorim. 2022: 1–8.
46. Zhao Y, Wang S, Liu Y, Song XX, Chen H, Zhang XM, Lin YH, Wang XL. Molecular modeling and reactivity of thermally altered coals by molecular simulation techniques. Energy Fuels. 2021;35(19):15663–74.
47. Solum MS, Pugmire RJ, Grant DM. Carbon–13 solid–state NMR of Argonne–premium coals. Energy Fuels. 1989;3(2):187–93.
48. Liu JX, Jiang YZ, Yao W, Jiang X, Jiang XM. The molecular characterization of Henan anthracite coal. Energy Fuels. 2019;33:6215–25.
49. Wang Q, Pan S, Bai JR, Chi MS, Cui D, Wang ZC, Liu Q, Xu F. Experimental and dynamics simulation studies of the molecular modeling and reactivity of the Yaojie oil shale kerogen. Fuel. 2018;230:319–30.
50. Okolo GN, Neomagus HWJP, Everson RC, Roberts MJ, Bunt JR, Sakurovs R, Mathews JP. Chemical–structural properties of South African bituminous coals: Insights from wide angle XRD–carbon fraction analysis, ATR–FTIR, solid state ^{13}C NMR, and HRTEM techniques. Fuel. 2015;158:779–92.
51. Kalaitzidis S, Georgakopoulos A, Christanis K, Iordanidis A. Early coalification features as approached by solid state ^{13}C CP/MAS NMR spectroscopy. Geochim Cosmochim Acta. 2006;70:947–59.
52. Tian B, Qiao YY, Bai L, Liu FJ, Tian YY, Xie KC. Separation and structural characterization of groups from a high–volatile bituminous coal based on multiple techniques. Fuel Process Technol. 2017;159:386–95.
53. Tong JH, Han XX, Wang S, Jiang XM. Evaluation of structural characteristics of Huadian oil shale kerogen using direct techniques (Solid–State ^{13}C NMR, XPS, FT–IR, and XRD). Energy Fuels. 2011;25:4006–13.

54. Song Y, Zhu YM, Li W. Macromolecule simulation and CH_4 adsorption mechanism of coal vitrinite. Appl Surf Sci. 2017;96:291–302.
55. Zhou Q. Study on occurrence mode of sulfur and nitrogen in coal in China. Clean Coal Technol. 2008;14:73–7 ((**in Chinese**)).
56. Takanohashi T, Kawashima H. Construction of a model structure for Upper Freeport coal using ^{13}C NMR chemical shift calculations. Energy Fuels. 2002;16:379–87.
57. Lille Ü, Heinmaa I, Pehk T. Molecular model of Estonian kukersite kerogen evaluated by ^{13}C MAS NMR spectra. Fuel. 2003;82(7):799–804.
58. Saha B, Schatz GC. Carbonization in polyacrylonitrile (PAN) based carbon fibers studied by ReaxFF molecular dynamics simulations. J Phys Chem B. 2012;116(15):4684–92.
59. Wang HJ, Feng YH, Zhang XX, Lin W, Zhao YL. Study of coal hydropyrolysis and desulfurization by ReaxFF molecular dynamics simulation. Fuel. 2015;145:241–8.
60. Chen SY, Ding JX, Li GY, Wang JP, Tian Y, Liang YH. Theoretical study of the formation mechanism of sulfur-containing gases in the CO_2 gasification of lignite. Fuel. 2019;242:398–407.
61. Fletcher TH, Kerstein AR, Pugmire RJ, Solum MS, Grant DM. Chemical percolation model for devolatilization3 Direct use of C–13 NMR data to predict effects of coal type. Energy Fuels. 1992;6(4):414–31.
62. Zhang ZJ, Guo LT, Zhang HY, Zhan JH. Comparing product distribution and desulfurization during direct pyrolysis and hydropyrolysis of Longkou oil shale kerogen using reactive MD simulations. Int J Hydrogen Energ. 2019;44(47):25335–46.
63. Zheng M, Li XX, Wang MJ, Guo L. Dynamic profiles of tar products during Naomaohu coal pyrolysis revealed by large–scale reactive molecular dynamic simulation. Fuel. 2019;253:910–20.
64. Sun XG. A study of chemical structure in "barkinite" using time of flight secondary ion mass spectrometry. Int J Coal Geol. 2001;47:1–8.
65. Sun XG. The optical features and hydrocarbon-generating model of "barkinite" from Late Permian coals in South China. Int J Coal Geol. 2002;51:251–61.
66. Dai HW, Chen NS, Liu NQ, Chen WM. Macerals and physicochemical properties of Loping bark coal. J China Coal Soc. 1984;3:81–7 ((**in Chinese**)).
67. Ouchi K, Itoh S, Makabe M, Itoh H. Pyridine extractable material from bituminous coal, its donor properties and its effect on plastic properties. Fuel. 1989;68(6):735–40.